Acta Pharmaceutica Sinica B 2026;16(6):3828−3845

Chinese Pharmaceutical Association
Institute of Materia Medica, Chinese Academy of Medical Sciences

Acta Pharmaceutica Sinica B

www.elsevier.com/locate/apsb
www.sciencedirect.com

ORIGINAL ARTICLE

Structural characterization of emulsion-type cataplasms with cross-linked networks and systematic establishment of structural parameters

Peng Yan[a], Ying Zhou[a,d], Hailong Zhang[b,c], Jinsong Ding[a,b,c,*]

[a]*Xiangya School of Pharmaceutical Sciences, Central South University, Changsha 410013, China*
[b]*Changsha Jingyi Pharmaceutical Technology Co., Ltd., Changsha 410205, China*
[c]*Hunan Engineering Research Center of Transdermal Drug Delivery Systems, Changsha 410205, China*
[d]*School of Life Science and Technology, Harbin Institute of Technology, Harbin 150001, China*

Received 8 September 2025; received in revised form 27 October 2025; accepted 2 November 2025

KEY WORDS

Emulsion-type cataplasms;
Characterization;
Structural parameters;
Cross-linked networks;
Formability;
Adhesion;
Four levels;
Industrial development

Abstract Compared with conventional cataplasms, those incorporating a cross-linked network structure significantly enhance their mechanical strength and cohesion, endowing them with good formability and adhesion properties, solving problems such as cold flow and slippage, thereby greatly increasing the convenience of use. However, systematic studies investigating the structural profiling of cross-linked networks in cataplasms remain scarce, limiting a comprehensive understanding of their functional significance. Therefore, we developed a systematic methodology to characterize emulsion-type cataplasms (as a model formulation) with cross-linked network structures, classifying their key structural parameters into four levels. The primary structures defined formability and adhesion, ensuring intact and durable skin adhesion. The secondary structure was intermediates formed by the drug and oily components. The tertiary structure was a dynamic structure, evaluating the quality changes of cataplasms during processes such as crosslinking and storage. The quaternary structure was a molecular structure, representing the mechanism by which the cross-linked network structure was formed. The factors influencing structural parameters and the laws between the intrinsic structures were investigated. Furthermore, we established threshold values for the primary structures, indicating when cataplasms possess optimal formability. This study offers new insights for cataplasm design and provides valuable references for industrial development.

*Corresponding author.
E-mail address: dingjs0221@csu.edu.cn (Jinsong Ding).

Peer review under the responsibility of Chinese Pharmaceutical Association and Institute of Materia Medica, Chinese Academy of Medical Sciences.

https://doi.org/10.1016/j.apsb.2025.12.046
2211-3835 © 2026 The Authors. Published by Elsevier B.V. on behalf of Chinese Pharmaceutical Association and Institute of Materia Medica, Chinese Academy of Medical Sciences. This is an open access article under the CC BY-NC-ND license (http://creativecommons.org/licenses/by-nc-nd/4.0/).

© 2026 The Authors. Published by Elsevier B.V. on behalf of Chinese Pharmaceutical Association and Institute of Materia Medica, Chinese Academy of Medical Sciences. This is an open access article under the CC BY-NC-ND license (http://creativecommons.org/licenses/by-nc-nd/4.0/).

1. Introduction

Cataplasms are a kind of topical preparation made by mixing drugs with hydrophilic substrates and then applying them onto backing materials[1]. Early cataplasms are non-crosslinked types with low formability, prone to phenomena such as cold flow and slippage, which could easily lead to paste residue on the skin and clothes[2,3], greatly reducing the convenience of use[4]. The free metal ions in the current cataplasms coordinated with the carboxylate ions in the gel skeleton and further physically cross-linked into a network structure[3,5,6], which obviously improves its mechanical strength and cohesion[7], gives it good formability and balanced adhesion, and solves the above problems. It is worth noting that compared with oral and intravenous administration, cataplasms have the advantages of non-invasiveness, good compatibility with skin, convenient administration, avoiding the first-pass effect and gastrointestinal irritation, etc.[8,9], thereby being widely used in the field of anti-inflammatory and analgesic in the clinic[10–12]. In order to deeply understand the characteristics of cataplasms, structural characterization based on the crosslinked network is particularly important. However, there is a lack of systematic studies on the crosslinked network structure of cataplasms.

Zhang et al.[13] propose that the structures of preparations are classified into four levels from macroscopic to molecular level based on structural pharmaceutics, especially in solid dosage forms. The four levels are composed of primary structure (dosage form or substructure), secondary structure (intermediate), tertiary structure (dynamic structure), and quaternary structure (molecular structure). For instance, the analysis of porosity, curvature and permeability in the membrane structure of the primary structure of controlled-release particles[14], the detection of particle size, volume and sphericity in the intermediate particle structure of the secondary structure of metoprolol succinate sustained-release tablets[15], the changes of the erosion layer, expansion layer and diffusion layer in the dynamic structure of the tertiary structure of felodipine extended release tablets[16], and the exploration of self-assembly film formation through electrostatic interaction simulation of the *in vitro* hydration kinetics of the quaternary structure of controlled-release matrix tablets[17], can provide a fundamental and in-depth understanding of the characteristics or functions of the preparations. There are many types of excipients and preparation processes for cataplasms, resulting in numerous structural changes and high analysis difficulty[18]. Especially, its secondary structure is not easy to characterize. However, the drug and oily components form emulsion droplets that are uniformly dispersed in emulsion-type cataplasms[19], which makes it feasible to characterize the four-level structure of emulsion-type cataplasms based on structural pharmaceutics.

Thus, we established methods to systematically characterize the structures of emulsion-type cataplasms with cross-linked networks and classify its structural parameters into four levels. The primary structures were maximum withstand force ($Force_{max}$, including $Force_{max}$ of paste ($Force_{max\text{-}mid}$) and cataplasms ($Force_{max\text{-}cat}$)), mean storage modulus of the linear viscoelastic region ($Mean_{G'\text{-}LVR}$), and mesh rate, which are obtained by a texture analyzer, rheometer, and scanning electron microscope (SEM), respectively, together representing the formability of cataplasms. In addition, as a topical preparation, one of the prerequisites for the therapeutic effect of cataplasms was its intact adherence to the skin surface for drug delivery[20,21]. Therefore, its adhesion was also categorized into the primary structures. The secondary structure was intermediates formed by drug and oily components, ensured by SEM combined with an energy-dispersive spectrometer (EDS). The time-dependent dynamic variation of $Mean_{G'\text{-}LVR}$, $Force_{max\text{-}mid}$, and $Force_{max\text{-}cat}$ reflected crosslinking degree and stability. These parameters were defined as tertiary structure to evaluate formulation quality. The quaternary structure was a molecular structure, which revealed the mechanism of crosslinked network structure formation of cataplasms by ultraviolet and visible spectrum (UV−Vis), attenuated total reflectance Fourier-transform infrared spectroscopy (ATR-FTIR), X-ray photoelectron spectroscopy (XPS), simulation, and SEM-EDS. In addition, the factors affecting the structural parameters, including formulations and storage conditions, and the laws between the intrinsic structures, were investigated. This study is expected to provide new insights for the design of cataplasms, bring new references for formulation design, adjustment, and quality evaluation, as well as promote the development of cataplasms industrialization.

2. Materials and methods

2.1. Materials

Flurbiprofen cataplasms (Zepolas®) were purchased by Beijing Tide Pharmaceutical Co., Ltd. (Beijing, China). Flurbiprofen and titanium dioxide were purchased by Hunan Jiudian Pharmaceutical Co., Ltd. (Changsha, China). Glycerin was purchased by Shandong Ruisheng Pharmaceutical Excipients Co., Ltd. (Liaocheng, China). Sodium carboxymethylcellulose (CMC-Na) was purchased by Ashland (Kentucky, USA). Kaolinite was purchased by Katsumitsuyama Mining Co., Ltd. (Tokyo, Japan). Gelatin was purchased by Guangdong Rousselot Gelatin Co., Ltd. (Guangzhou, China). Disodium edetate (EDTA-2Na) and tartaric acid (TA) were purchased from Nanjing Chemical Reagent Co., Ltd. (Nanjing, China). Tween 80 was purchased by Nanjing Well Pharmaceutical Technology Co., Ltd. (Nanjing, China). Span 80 was purchased by Guangdong Runhua Chemical Co., Ltd. (Qingyuan, China). Sodium polyacrylate NP700 and NP600 were purchased by RESONAC (Tokyo, Japan). Aluminum glycinate was purchased by Kyowa Chemical Industry Co., Ltd. (Tokyo, Japan). Polyvinyl alcohol was purchased by Jiangxi Alpha Hi-tech Pharmaceutical Co., Ltd. (Pingxiang, China). L-Menthol was purchased by Takasago International Corporation (Tokyo, Japan).

2.2. Preparation of matrix and cataplasms

TA and water were added to a 10 mL beaker and stirred until dissolved to obtain the water phase. Aluminum glycinate, EDTA-2Na, sodium polyacrylate, and glycerin were added to a 25 mL beaker and stirred thoroughly to obtain the oil phase. Then the water phase was poured into the oil phase and stirred for 30 min to

obtain the matrix. The amount of each component in the matrix was detailed in Supporting Information Tables S1-S4.

TA, gelatin, polyvinyl alcohol, and water were added to a 1000 mL beaker and stirred at a stirring speed of 800 revolutions per minute (rpm) (SHJ-6A, JTLIANGYOU Instrument Co., Ltd., Changzhou, China) until dissolved at 80 °C to obtain the water phase[22–24]. Flurbiprofen, Span 80, Tween 80, and L-menthol were added to a 25 mL beaker and stirred at a stirring speed of 400 rpm

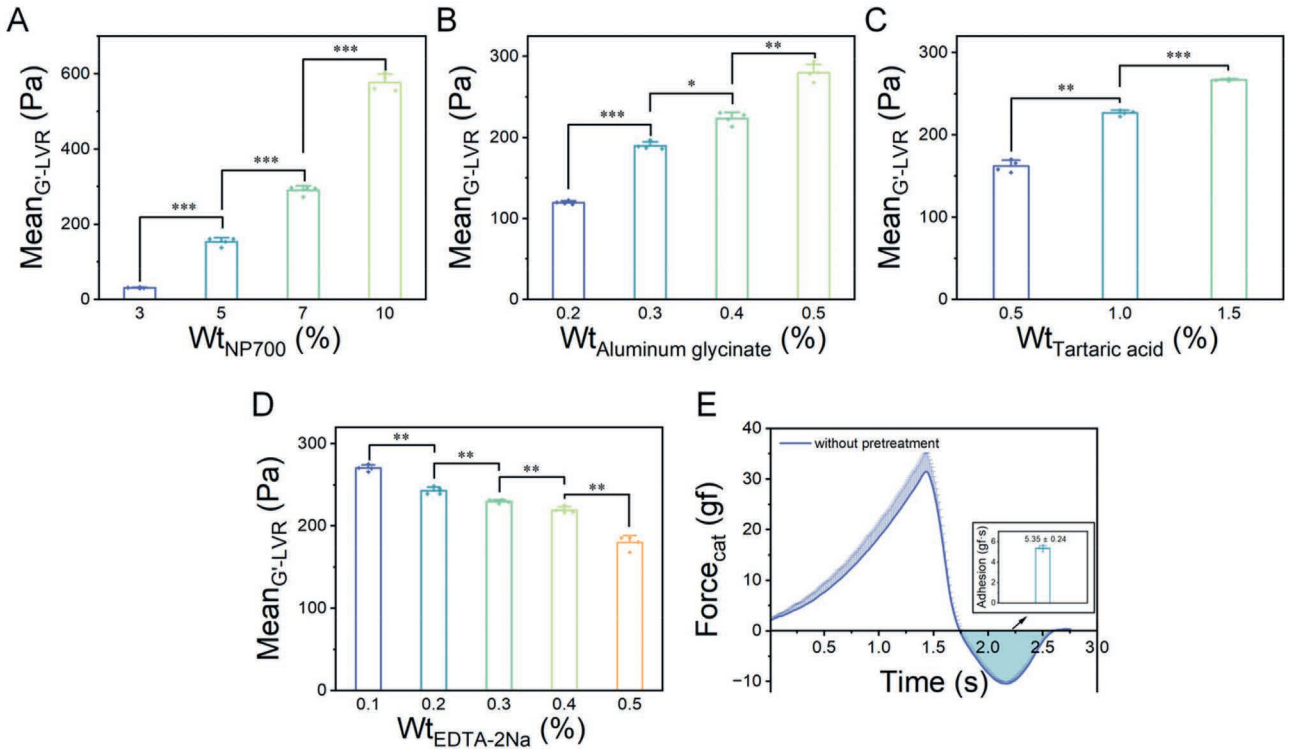

Figure 1 Mean$_{G'\text{-LVR}}$ and Force$_{cat}$ of primary structures in cataplasms. Mean$_{G'\text{-LVR}}$ of matrix with different (A) NP700, (B) aluminum glycinate, (C) TA, and (D) EDTA-2Na dosages. (E) Force$_{cat}$ and adhesion of Zepolas® detected at the site without pretreatment. The data are expressed as mean ± SD. One-way ANOVA was applied for comparisons. $n = 4$. *, **, and *** represented $P < 0.05$, $P < 0.01$, and $P < 0.001$, respectively.

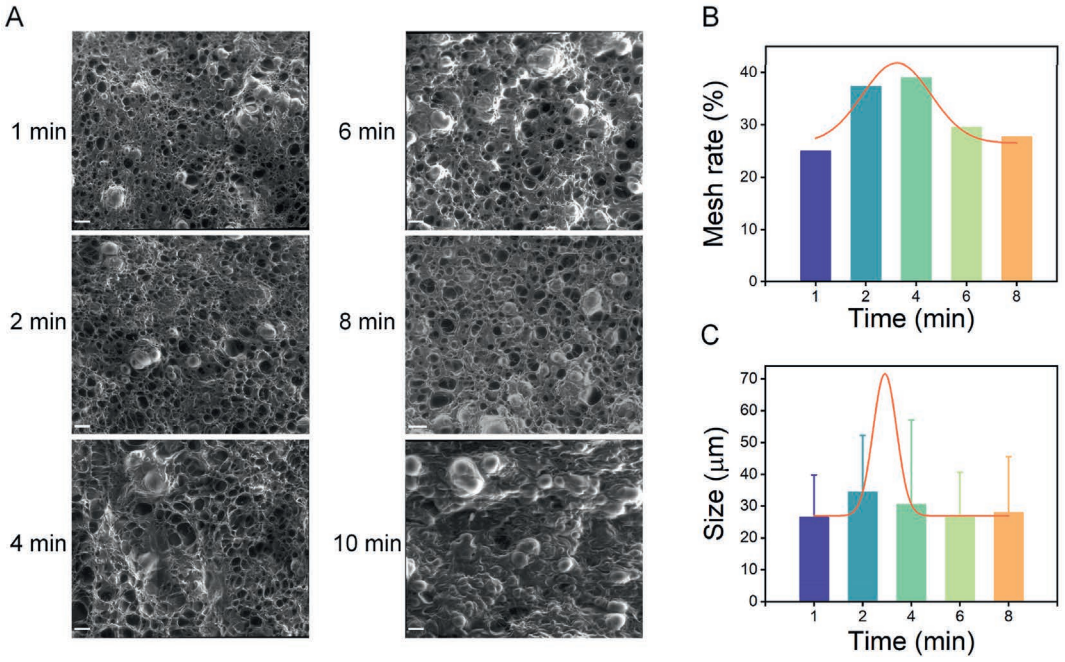

Figure 2 Characterization of cataplasms by SEM after swelling and freeze-drying. (A) SEM images, (B) mesh rate, and (C) mesh size of cataplasms at different swelling times. Scale bar = 200 μm.

(CJB-S180, Yuhua Instrument Co., Ltd., Gongyi, Henan, China) until dissolved to obtain the active pharmaceutical ingredient (API) phase. Sodium polyacrylate, aluminum glycinate, EDTA-2Na, CMC-Na, kaolinite, titanium Dioxide, and glycerin were added to a 1000 mL beaker and stirred at a stirring speed of 800 rpm (RW 20 D S025, IKA-Werke GmbH & Co. KG, Staufen, Baden-Württemberg, Germany) for 30 min to obtain the oil phase. The API phase was first poured into the oil phase and stirred at a stirring speed of 800 rpm for 30 min. Then the mixture was transferred to a stirring pot, and the water phase was added and stirred at a stirring speed of 50 rpm (HD-PZ4L, Xinyi Huida Mechanical & Electrical Equipment Co., Ltd., Fangshan, Beijing, China) for 30 min to obtain the paste. Finally, cataplasms were obtained by a coater (HD-SIII, Xinyi Huida Mechanical & Electrical Equipment Co., Ltd., Fangshan, Beijing, China) with a coating thickness of about 1.00 mm[25]. The details of formations in cataplasms were shown in Supporting Information Tables S5-S9.

2.3. *Characterization of primary structures*

2.3.1. *Force$_{max}$ and adhesion*

Force$_{max\text{-}mid}$ and Force$_{max\text{-}cat}$ were detected by a texture analyzer (XTC, Shanghai Baosheng Industrial Development Co., Ltd., Songjiang, Shanghai, China)[26,27]. Briefly, as shown in Supporting Information Fig. S1, the samples were placed on the sample stage of the texture analyzer, followed by the testing conditions according to Supporting Information Table S10. Force$_{max}$ and adhesion were further obtained by analysis and calculation[28,29].

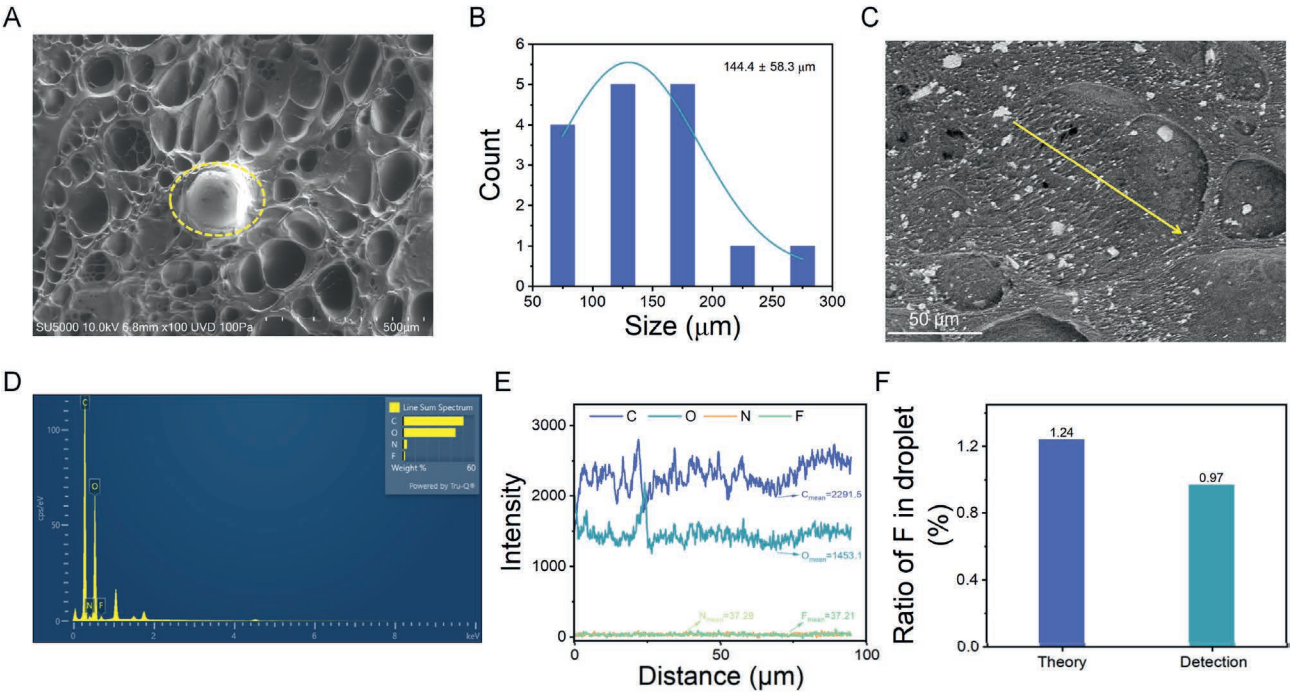

Figure 3 Characterization of secondary structures in cataplasms. (A) Images of cataplasms characterized by SEM at UVD mode. (B) Size of spherical droplets in cataplasms after swelling and freeze-drying. (C) Images of cataplasms characterized by SEM at BSE mode. Scale bar = 50 μm. (D) Element signal diagram detected by SEM-EDS. (E) Element signal intensity. (F) Ratio of F in droplet.

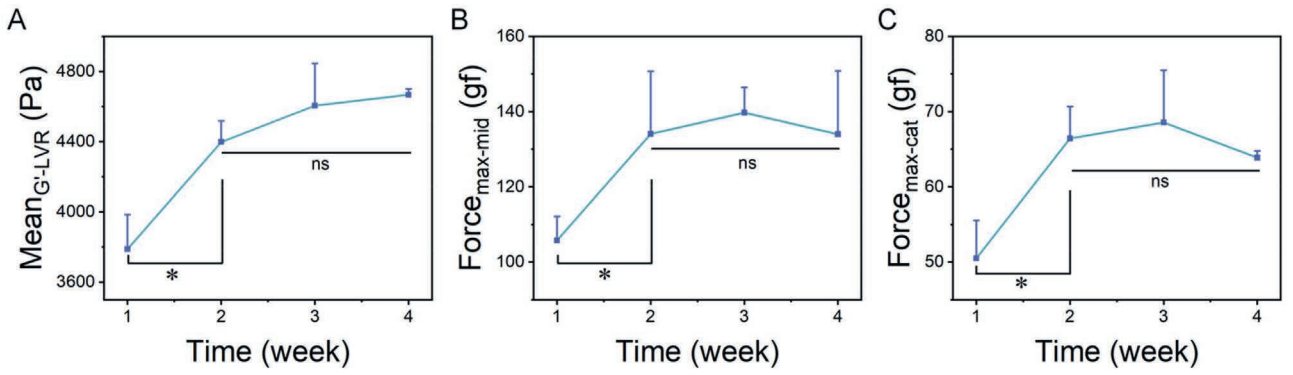

Figure 4 Characterization of tertiary structure in cataplasms. Variation of (A) Mean$_{G'\text{-}LVR}$, (B) Force$_{max\text{-}mid}$, and (C) Force$_{max\text{-}cat}$ of cataplasms within 4 weeks. The data are expressed as mean ± SD. One-way ANOVA was applied for comparisons. $n = 4$. ns and * represented $P > 0.05$ and $P < 0.05$, respectively.

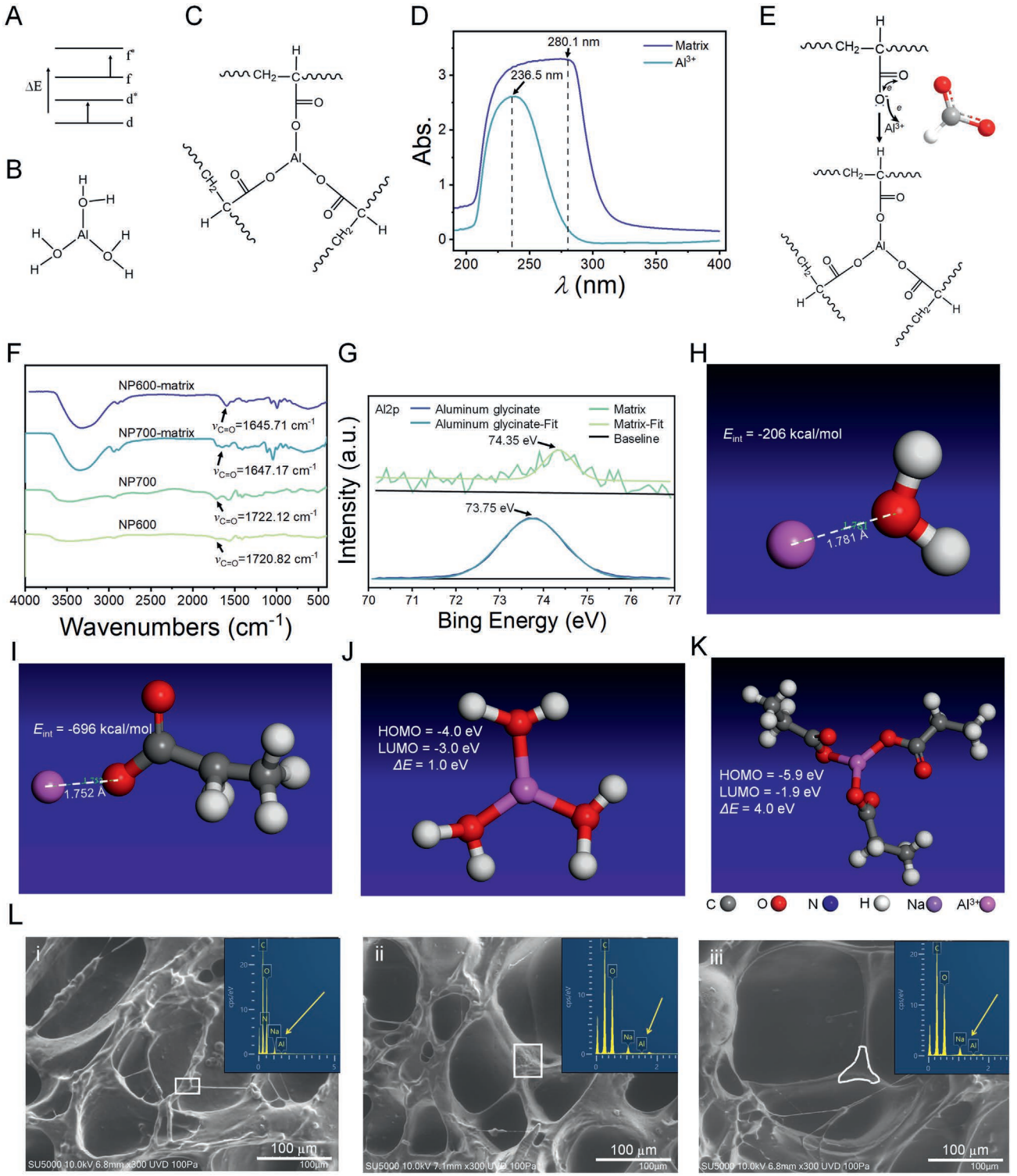

Figure 5 Characterization of quaternary structures in cataplasms. (A) Types of electronic transitions in coordination compounds. The structure of the coordination compound formed by Al^{3+} and (B) water or (C) $-COO^{-}$. (D) UV−vis absorption curve of the coordination compound formed by Al^{3+} and water or $-COO^{-}$. (E) Brief schematic diagram of electron transfer in the formation of coordination compounds. (F) IR curve of sodium polyacrylate and matrix. (G) XPS spectra of the matrix and aluminum glycinate. Molecular docking between Al^{3+} and (H) H_2O or (I)$-COO^{-}$. The coordinated compound orbital simulation between Al^{3+} and (J) H_2O or (K) $-COO^{-}$. (L) SEM-EDS images. i, ii, and iii represented the images of three different regions.

2.3.2. $Mean_{G'\text{-}LVR}$

G' was detected by rheometer (Discovery, TA Instruments, Newcastle, Delaware, USA)[25]. Briefly, as shown in Supporting Information Fig. S2, the samples were placed on the sample stage of the texture analyzer, followed by the testing conditions according to Supporting Information Table S11. $Mean_{G'\text{-LVR}}$ was further obtained by analysis.

2.3.3. Mesh rate

Briefly, cataplasms were put in purified water to swell for 1, 2, 4, 6, 8, and 10 min[30]. Then it was transferred to a vacuum freeze dryer for 48 h to obtain the pretreated cataplasms. Next, its morphology was observed by SEM (SU5000, Hitachi High-Tech Co., Ltd., Marunouchi, Tokyo, Japan) in low vacuum and ultra variable-pressure detector mode at an accelerating voltage of 10 kV. Finally, the mesh rate was analyzed by Image J (154, National Institutes of Health, Bethesda, Maryland, USA).

2.4. Characterization of secondary structure

Briefly, as shown in Supporting Information Fig. S3, the pretreated cataplasms were milled on the surface by a soft ion polisher, followed by SEM in low vacuum back scattered electron mode under accelerating voltage conditions of 10 kV to find the field of view of the structural unit formed by drug intermediates and crosslinking networks[31]. Then the drug intermediates were analyzed by EDS for their elemental compositions and distributions.

2.5. Characterization of tertiary structures

The tertiary structures referred to the change of $Mean_{G'\text{-LVR}}$, $Force_{max\text{-}mid}$, and $Force_{max\text{-}cat}$ over time.

2.6. Characterization of quaternary structure

2.6.1. UV−vis

The samples were placed in a quartz dish and were measured by UV−Vis (UV-2600i, Shimadzu Corporation, Nishinokyo, Kyoto, Japan) at 180−400 nm to obtain the maximum absorption wavelength[32].

2.6.2. ATR-FTIR

The samples to be tested were uniformly covered on the surface of ATR crystals. Then the spectra were collected by ATR-FTIR (IRAffinity-1S, Shimadzu Corporation, Nishinokyo, Kyoto, Japan) at the wave number range of 4000−400 cm^{-1}, with scan times of 50 and the angle of incidence fixed at 45° to ensure optimal attenuation total reflection conditions[33].

2.6.3. XPS

XPS of the samples was measured by a spectrometer (K-Alpha, Thermo Scientific, Waltham, Massachusetts, USA)[34]. The samples were placed on the sample holder and transferred into the analysis chamber under vacuum conditions for testing. The detection parameters were as follows: Al Kα as the excitation source, a beam spot size of 400 μm, an operating voltage of 12 kV, a filament current of 6 mA, and a full-spectrum scan with a pass energy of 150 eV and a step size of 1 eV.

2.6.4. Simulation

Firstly, the structures of Al, H_2O, NP700 monomer, and EDTA-2Na were drawn in Materials Studio (2020, BIOVIA, Vélizy-Villacoublay, Yvelines, France). Then the corresponding charge parameters were set under Generalized Gradient Approximation and Perdew-Burke-Ernzerhof conditions in $Dmol^3$ mode[35,36]. Each structure was optimized geometrically before molecular docking. The binding energy (E_{int}) was obtained by calculation and analysis.

Similarly, the structures of $Al(H_2O)_3$, $Al(NP700\ monomer)_3$ were drawn in Materials Studio. Then the corresponding charge parameters were set for each structure in $Dmol^3$ mode, followed by geometry optimization and energy simulation. The Highest occupied molecular orbital and lowest unoccupied molecular orbital data were obtained, and their energy differences were further calculated[37,38]. Higher energy differences meant that the complex was more stable.

2.7. Statistical analysis

All data were analyzed using one-way ANOVA or Student's *t*-test in Origin (2025 Learning Edition, OriginLab Corporation, Northampton, Massachusetts, USA)[39]. $P > 0.05$ indicated no significant difference among groups (ns). $P < 0.05$, $P < 0.01$, and $P < 0.001$, indicated significant difference (*), very significant difference (**), and extremely significant difference (***) among groups, respectively. The data are expressed as mean ± SD.

3. Results and discussion

3.1. Establishment of structural parameters

3.1.1. Primary structures

Generally speaking, LVR was at a constant plateau, reflecting that its molecular structure was stable and was not easy to be disrupted[40]. As shown in Fig. 1A, when the dosage of NP700 increased from 3% to 10%, $Mean_{G'\text{-LVR}}$ correspondingly rose from 30.9 ± 1.7 Pa to 576.8 ± 23.0 Pa. This was due to the increase in the number of ligands in the matrix, which in turn led to an increase in the degree of crosslinking. The stress range in the LVR first increased, then remained unchanged, and continued to increase (Supporting Information Tables S12−S15), resulting from G' was positively correlated with the ratio of stress to strain. Even if the stress did not change significantly, the strain showed a decreasing trend, meaning that the change of G' could remain at an increasing level. It was observed from Fig. 1B and C that with the increase in the dosage of the crosslinking agent-aluminum glycinate, and the pH modifier-TA, $Mean_{G'\text{-LVR}}$ also maintained an increasing trend. This was attributed to the increase in the number of central atoms, contributing to an increase in the crosslinking degree of the matrix. In addition, with a fivefold increase in crosslinking regulator-EDTA-2Na dosage, $Mean_{G'\text{-LVR}}$ decreased by 34% (Fig. 1D). This was ascribed to EDTA-2Na acting as a competitive ligand that chelated with Al^{3+}, giving rise to a decrease in the degree of crosslinking of the matrix. It was worth noting that there was no regularity in the changes of loss modulus and phase angle (Supporting Information Fig. S4), preliminarily indicating that the $Mean_{G'\text{-LVR}}$ detected by the rheometer had a certain degree of discrimination as a structural parameter and could reflect the strength of the cross-linked network structure.

The cross-linked network structure of cataplasms enhanced its cohesion, providing a certain degree of resistance to externally induced deformation. As depicted in Supporting Information Fig. S5, $Force_{cat\text{-}max}$ of Zepolas® measured *in situ* with back

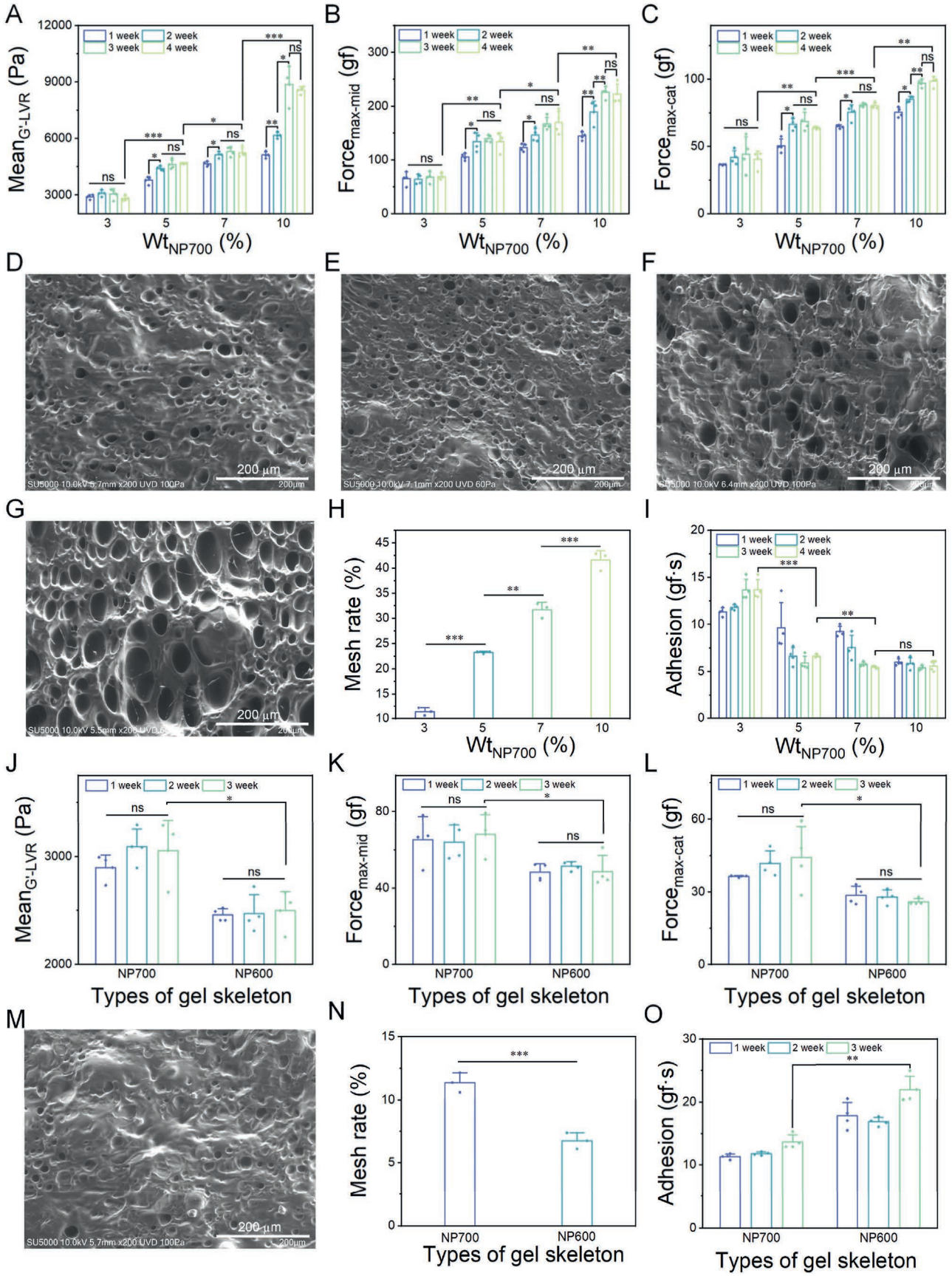

Figure 6 Structural characterization of cataplasms with different gel skeletons. Variation of (A) $Mean_{G'\text{-}LVR}$, (B) $Force_{max\text{-}mid}$, (C) $Force_{max\text{-}cat}$, and (H) mesh rate of cataplasms with different NP700 dosages within 4 weeks. SEM images of cataplasms with (D) 3%, (E) 5%, (F) 7%, and (G)

membrane solidification was 45.9 ± 13.5 gf, with a large variation, which might be caused by the difference in the solidification degree. Notably, $Force_{cat\text{-}max}$ of Zepolas® detected *in situ* without pretreatment was 32.9 ± 2.8 gf, with minimal error (Fig. 1E). Meanwhile, the adhesion was calculated as 5.4 ± 0.2 gf·s.

Supporting Information Fig. S6 displayed that Zepolas® did not exhibit a cross-linked network structure, with freeze-drying treatment or without pretreatment. Fortunately, Zepolas® had a clear cross-linked network structure after swelling and freeze-drying pretreatment. As illustrated in Fig. 2, both the mesh rate and mesh size first increased and then decreased with prolonged swelling time, eventually stabilizing at a constant level. This was likely due to the cross-linked network structure first swelling and then contracting to reach equilibrium. Notably, prolonged swelling time led to noticeable droplet aggregation, which was speculated to be caused by interactions between droplets. This suggested that a pretreatment method combining 2 min of swelling followed by freeze-drying was proposed to be selected, as it could characterize the cross-linked network structure while minimizing structural damage. Additionally, given that the changing trends of mesh rate and mesh size were similar, the mesh rate was proposed as the parameter for the primary structure.

3.1.2. Secondary structures

The secondary structure represented intermediates formed by the drug and oily components in cataplasms. As shown in Fig. 3A and B, Zepolas® not only exhibited a clear cross-linked network structure, but also had spherical droplets with a particle size of 144.4 ± 58.3 μm. After milling the surface of the preparation with a soft ion beam, the F element signal was detected in the droplet by SEM-EDS, preliminarily confirming that the droplet was a drug intermediate (Fig. 3C and D). Semi-quantitative analysis and calculations showed that the average intensity value of F element detection was close to the actual molar proportion (Fig. 3E and F), which demonstrated the feasibility of this method for characterizing the secondary structure of cataplasms. Element identification relied on characteristic X-rays emitted when atoms are bombarded by an electron beam, which are captured by EDS. Elements with high atomic numbers exhibited stronger signal intensities due to higher X-ray yields and lower background interference, enabling a detection accuracy of 0.1% under optimized conditions[41]. Notably, if the drug in cataplasms lacks detectable distinctive elemental signatures, EDS analysis would fail—a key limitation of this technique.

3.1.3. Tertiary structures

The tertiary structure was a dynamic structure, assessing the quality of cataplasms. As illustrated in Fig. 4, compared with the initial time point (week 1), $Mean_{G'\text{-}LVR}$, $Force_{max\text{-}mid}$, and $Force_{max\text{-}cat}$ at week 2 exhibited significant increases from 3788.3 ± 196.4 Pa, 105.8 ± 6.4 gf, and 50.5 ± 5.1 gf to 4397.9 ± 119.6 Pa, 134.1 ± 16.7 gf, and 66.4 ± 4.2 gf, respectively. This synchronous growth pattern indicated substantial crosslinked network formation during this period. Notably, these parameters reached a plateau phase after week 2, demonstrating that the crosslinking reaction had achieved a dynamic equilibrium state. Based on these dynamic changes, the optimal maturation time of cataplasms was initially determined to be 2 weeks. This conclusion was grounded in quantitative analysis rather than traditional empirical judgment or qualitative analysis. The time-dependent tertiary structure parameters provided a scientific basis for process control in pharmaceutical manufacturing.

3.1.4. Quaternary structure

The quaternary structure was the molecular structure of the formulation. The most important structure in cataplasms was the cross-linked network structure. Based on the relationship that structure determined performance[42], exploring the formation of this structure was of great significance for understanding the research and development of cataplasms. It was observed from Fig. 5A that the common transition types of central ions in coordination compounds were typically of two main types: d to d* and f to f*[43,44]. Although H_2O could serve as Al^{3+} ligands (Fig. 5B and C), $-COO^-$ had stronger electron-donating ability and higher electron density, requiring less energy for electronic transitions and thus forming bonds more easily. This results in a red shift of λ_{max} from 236.5 to 280.1 nm (Fig. 5D). Additionally, $-COO^-$ possessed a p-π conjugated structure (Fig. 5E). The addition of Al^{3+} caused electrons to move from −COO to Al^{3+}, resulting in a decrease in electron density on the carbonyl group, an increase in the dipole moment, leading to a blue shift of $\nu_{C=O}$ (Fig. 5F). As shown in Fig. 5G, XPS analysis revealed that the binding energies of Al in the matrix (Al2p at 74.35 eV) were significantly higher than those in aluminum glycinate (Al2p at 73.75 eV). This was because the electron cloud density of Al decreases, enhancing its electropositivity and thus providing further evidence for the coordination between O and Al. Therefore, the formation of the cross-linked network structure was based on the coordination bonding between Al^{3+} and the carboxylate ions ($-COO^-$) in polyacrylic acid. Molecular docking results show that the molecular distance and E_{int} between Al^{3+} and O in H_2O (1.781 Å and −206 kcal/moL) were smaller than that between Al^{3+} and $-COO^-$ (1.752 Å and −696 kcal/moL) (Fig. 5H and I). Additionally, through simulation analysis, the compound orbital energy of Al^{3+} binding with H_2O (1 eV) was lower than that of $-COO^-$ (4 eV), indicating that Al^{3+} was more readily coordinated with $-COO^-$ (Fig. 5J and K). Furthermore, as shown in Supporting Information Fig. S7, E_{int} between Al^{3+} and the N and O atoms in EDTA-2Na (−824 kcal/moL) was greater than that of $-COO^-$ (−696 kcal/moL) to avoid excessive cross-linking, thereby facilitating the coating process. Notably, as depicted in Fig. 5L, the central region of the cross-linked network structure contained Al elements, further confirming the mechanism of cross-linked network formation.

The establishment of primary, secondary, tertiary, and quaternary structures was conducive to understanding the existence of

10% NP700. (I) Changes of adhesion of cataplasms with different NP700 dosages within 4 weeks. Variation of (J) $Mean_{G'\text{-}LVR}$, (K) $Force_{max\text{-}mid}$, (L) $Force_{max\text{-}cat}$, and (N) mesh rate of cataplasms with different gel skeleton types within 3 weeks. (M) SEM images of cataplasms with NP600. (O) Changes in adhesion of cataplasms with different gel skeleton types within 3 weeks. The data are expressed as mean ± SD. Statistical analysis was performed using a Student's *t*-test for comparisons between two groups. One-way ANOVA was applied for comparisons involving three or more groups. $n = 4$. ns, *, **, and *** represented $P > 0.05$, $P < 0.05$, $P < 0.01$, and $P < 0.001$, respectively.

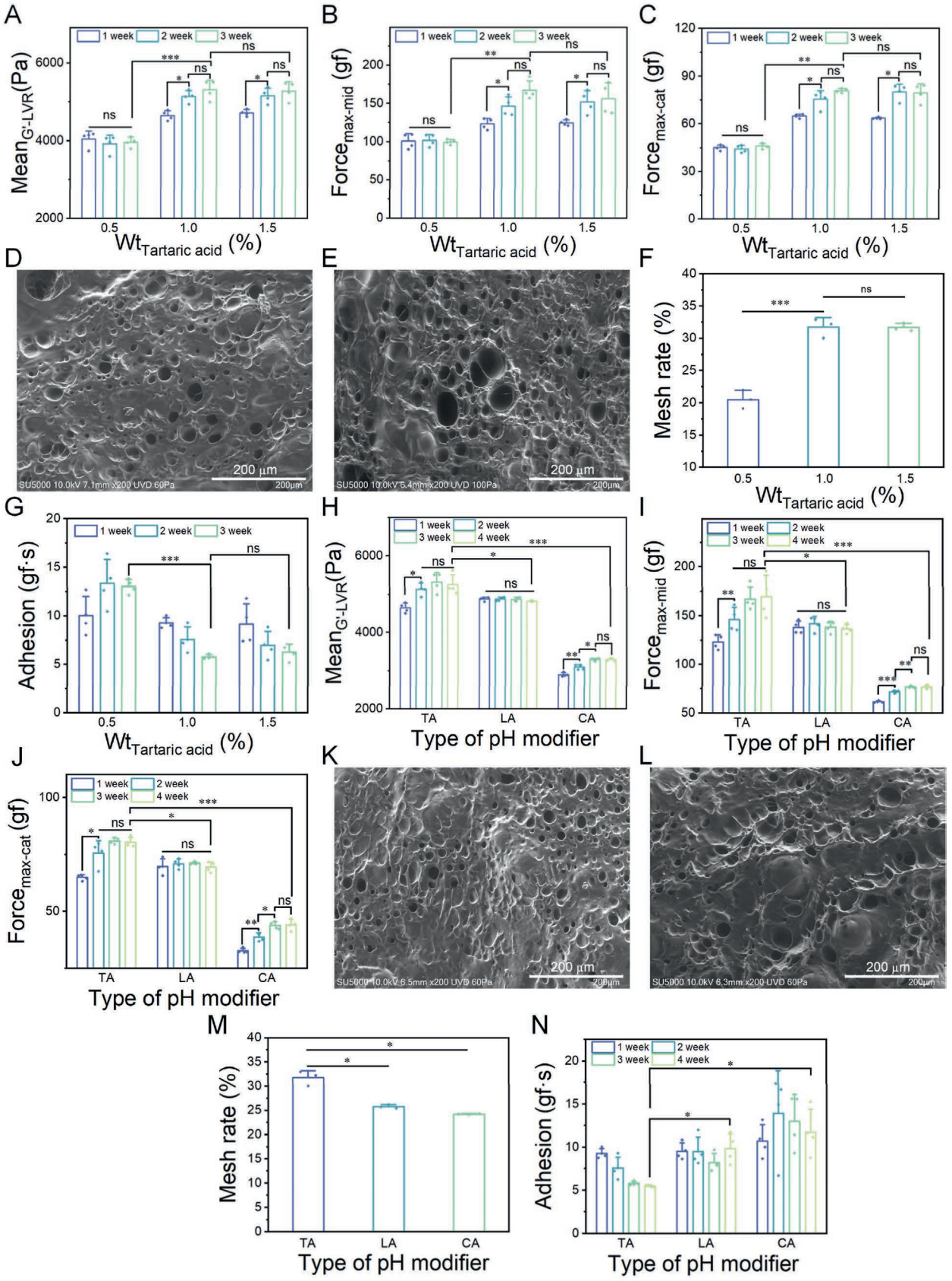

Figure 7 Structural characterization of cataplasms with different pH modifiers. Variation of (A) $Mean_{G'\text{-}LVR}$, (B) $Force_{max\text{-}mid}$, (C) $Force_{max\text{-}cat}$, and (F) mesh rate of cataplasms with different TA dosages within 3 weeks. SEM images of cataplasms with (D) 0.5% and (E) 1.5% TA. (G) Changes in adhesion of cataplasms with different TA dosages within 3 weeks. Variation of (H) $Mean_{G'\text{-}LVR}$, (I) $Force_{max\text{-}mid}$, (J) $Force_{max\text{-}cat}$, and

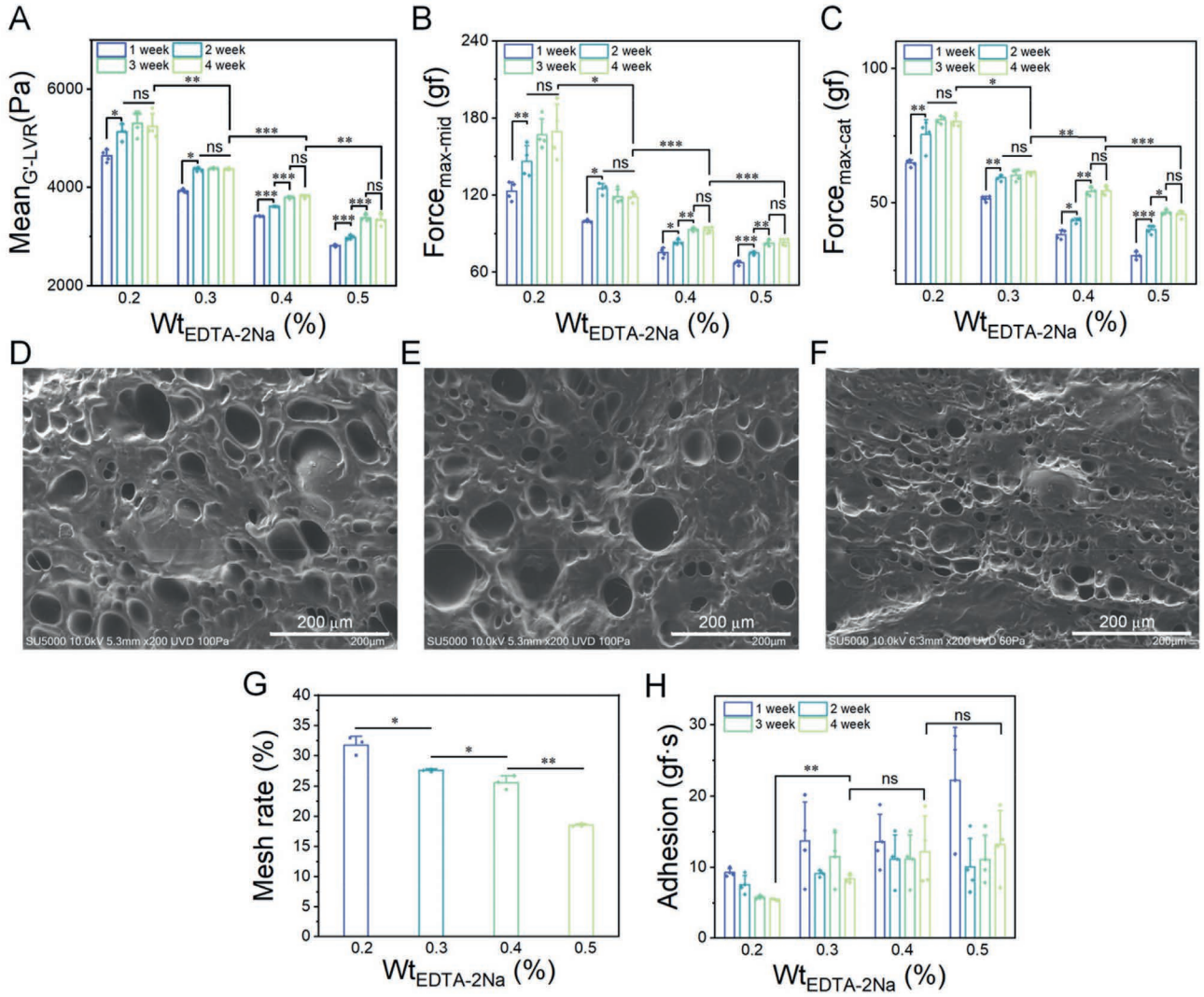

Figure 8 Structural characterization of cataplasms with different EDTA-2Na dosages. Variation of (A) Mean$_{G'\text{-LVR}}$, (B) Force$_{max\text{-}mid}$, (C) Force$_{max\text{-}cat}$, and (G) mesh rate of cataplasms with different EDTA-2Na dosages within 4 weeks. SEM images of cataplasms with (D) 0.3%, (E) 0.4%, and (F) 0.5% EDTA-2Na. (H) Changes in adhesion of cataplasms with different EDTA-2Na dosages within 4 weeks. The data are expressed as mean ± SD. One-way ANOVA was applied for comparisons. $n = 4$. ns, *, **, and *** represented $P > 0.05$, $P < 0.05$, $P < 0.01$, and $P < 0.001$, respectively.

cross-linked network structures in cataplasms from a macroscopic to molecular level, laying the foundation for subsequent investigations into the relationship between structure and performance.

3.2. *The effect of the key component on structure*

The cross-linked network structure of cataplasms was formed by the joint action of the gel skeleton, pH modifier, cross-linking regulator, and cross-linking agent. Meanwhile, the properties of the drug affect the formation of drug intermediates. Based on the structural parameter characterization method established in Section 3.1, the following would examine the effect of these five key components on structure.

3.2.1. *Gel skeleton*

As shown in Fig. 6A−H and Supporting Information Fig. S8, when the dosage of NP700 increases from 3% to 10% in cataplasms, Force$_{max\text{-}mid}$, Force$_{max\text{-}cat}$, Mean$_{G'\text{-LVR}}$, and mesh rate increased from 69.2 ± 5.5 gf to 222.8 ± 17.9 gf, 40.4 ± 6.3 gf to 98.5 ± 3.8 gf, 2812.5 ± 139.6 Pa to 8577.5 ± 187.0 Pa, and 11.3 ± 0.8% to 41.5 ± 1.9%, respectively. This was because an

(M) mesh rate of cataplasms with different pH modifier types within 4 weeks. SEM images of cataplasms with (K) LA and (L) CA. (N) Changes in adhesion of cataplasms with different pH modifier types within 4 weeks. The data are expressed as mean ± SD. One-way ANOVA was applied for comparisons. $n = 4$. ns, *, **, and *** represented $P > 0.05$, $P < 0.05$, $P < 0.01$, and $P < 0.001$, respectively.

increase in the amount of NP700 contributed to an increase in the number of ligands ($-COO^-$), thereby leading to an enhancement of the crosslinking degree. More importantly, the crosslinking completion time, as determined by these structural parameters, rose from 1 to 3 weeks (Supporting Information Table S16), delineating that cataplasms had fully matured and further providing guidance for its industrialization. It was observed from Fig. 6I that the adhesion of cataplasms first

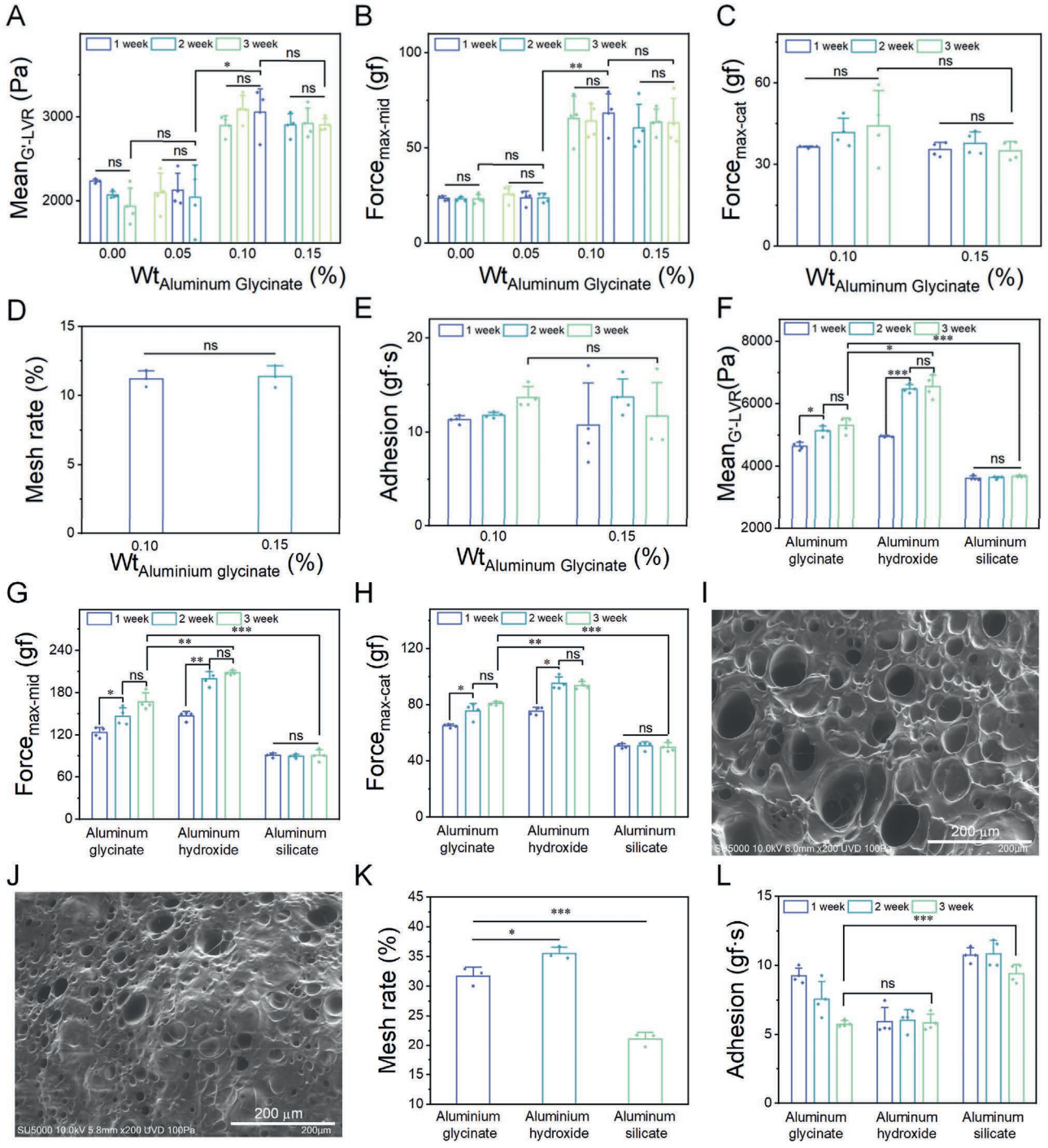

Figure 9 Structural characterization of cataplasms with different crosslinking agents. Variation of (A) $Mean_{G'\text{-}LVR}$, (B) $Force_{max\text{-}mid}$, (C) $Force_{max\text{-}cat}$, and (D) mesh rate of cataplasms with different aluminum glycolate dosages within 3 weeks. (E) Changes in adhesion of cataplasms with different aluminum glycolate within 3 weeks. Variation of (F) $Mean_{G'\text{-}LVR}$, (G) $Force_{max\text{-}mid}$, (H) $Force_{max\text{-}cat}$, and (K) mesh rate of cataplasms with different crosslinking agent types within 3 weeks. SEM images of cataplasms with (I) aluminum hydroxide and (J) aluminum silicate. (L) Changes in adhesion of cataplasms with different crosslinking agent types within 3 weeks. The data are expressed as mean ± SD. Statistical analysis was performed using a Student's *t*-test for comparisons between two groups. One-way ANOVA was applied for comparisons involving three or more groups. $n = 4$. ns, *, **, and *** represented $P > 0.05$, $P < 0.05$, $P < 0.01$, and $P < 0.001$, respectively.

decreased from 13.7 ± 1.1gf·s to 5.5 ± 0.1 gf·s and then remained unchanged. The former was due to the increase in crosslinking degree, enhancing cohesion and thereby reducing adhesion, while the latter was attributed to the presence of adhesive that cataplasms maintained a certain degree of adhesion.

Compared to NP700, NP600 had a higher sodium acrylate content (Supporting Information Table S17), theoretically meaning that it had a greater number of ligands and a higher degree of cross-linking. However, as outlined in Fig. 6J−N and Supporting Information Fig. S9A−S9G, $Force_{max\text{-}mid}$, $Force_{max\text{-}cat}$, $Mean_{G'\text{-}LVR}$, and mesh rate of NP700 were all higher than those of NP600. This might be because the pH of cataplasms with NP700 was lower than that with NP600 (Fig. S9H), which facilitated the dissociation of Al^{3+} in the crosslinking agent and enhanced the crosslinking degree. Moreover, cohesion and adhesion were a pair of balanced parameters. Therefore, even though cataplasms with NP600 furnished lower cohesion than those with NP700, its adhesion was higher than that of NP700 (Fig. 6O).

3.2.2. *pH modifier*

Fig. 7A−F and Supporting Information Fig. S10 displayed that doubling the amount of TA resulted in increases of 67.3%, 76.1%, 33.9%, and 54.4% in $Force_{max\text{-}mid}$, $Force_{max\text{-}cat}$, $Mean_{G'\text{-}LVR}$, and mesh rate, respectively. This was since the increase in the amount of TA promoted the dissociation of Al^{3+}, which led to an increase in the number of central atoms in the coordination complex, thus increasing the degree of cross-linking and the time for cross-linking of the formulation (Supporting Information Table S18). When the amount of TA was increased from 1.0% to 1.5%, $Force_{max\text{-}mid}$, $Force_{max\text{-}cat}$, $Mean_{G'\text{-}LVR}$, and mesh rate remained unchanged, resulting from limited Al^{3+} content in the cataplasms. The number of central atoms reached the upper limit. Even if the amount of tartaric acid was increased further, and crosslinking completion time and crosslinking degree remain unchanged. Correspondingly, as the amount of TA increased, the adhesion of cataplasms first decreased and then remained unchanged (Fig. 7G).

As shown in Fig. 7H and Supporting Information Fig. S11A, the relationship of $Mean_{G'\text{-}LVR}$ of the three organic acids was as follows: TA (dicarboxylic acid) > lactic acid (LA, monocarboxylic acid) > citric acid (CA, tricarboxylic acid). $Force_{max\text{-}mid}$, $Force_{max\text{-}cat}$, and mesh rate also followed the same trend (Fig. 7I−M and Fig. S11B−S11I). Generally speaking, the stronger the acidity of the pH modifier, the easier it was to dissociate Al^{3+}, which was conducive to the improvement of the degree of crosslinking. However, although CA was more acidic than LA (Fig. S11J and Supporting Information Table S19), the degree of cross-linking of cataplasms with CA was weaker than that with LA. This might be because tricarboxylic acid had more O atoms, thus having a stronger ability to compete for the complexation of Al^{3+}, which was unfavorable to the formation of cross-linking networks. Based on the presence of a tacky agent, there was no significant difference in adhesion between CA and LA (Fig. 7N).

3.2.3. *Cross-linking regulator*

It was observed from Fig. 8A−G and Supporting Information Fig. S12 that when the content of EDTA-2Na increased from 0.2% to 0.5% in cataplasms, $Force_{max\text{-}mid}$, $Force_{max\text{-}cat}$, $Mean_{G'\text{-}LVR}$, and mesh rate decreased from 169.5 ± 21.1 gf to 83.3 ± 2.7 gf, 80.3 ± 2.2 gf to 45.9 ± 1.3 gf, 5242.5 ± 257.5 Pa to 3342.5 ± 116.7 Pa, and 31.7 ± 1.5% to 18.5 ± 0.3%, respectively. EDTA-2Na acted as a competitive ligand, chelating Al^{3+} in cataplasms, thereby reducing the degree of crosslinking and prolonging the crosslinking time (Supporting Information Table S20). In addition, with the increase of EDTA-2Na, the cohesion of cataplasms decreased, giving rise to an initial increase in adhesion of the patch and then remaining unchanged (Fig. 8H). Most commercial cataplasms employed EDTA-2Na as a cross-linking regulator[45−52]. Therefore, based on actual conditions, only the dosage of the crosslinking regulator (EDTA-2Na) was examined here, without expanding to other types.

3.2.4. *Cross-linking agent*

As shown in Fig. 9A and B and Supporting Information Fig. S13A−S13D, when the dosage of aluminum glycinate was increased from 0 to 0.15%, both $Mean_{G'\text{-}LVR}$ and $Force_{max\text{-}mid}$ remained unchanged at first, then increased to 3057.5 ± 274.4 Pa and 68.3 ± 10.0 gf, respectively, and finally remained unchanged. It was speculated that the reason for this might be that the vast majority of free Al^{3+} in cataplasms was chelated by EDTA-2Na competition, resulting in a low degree of cross-linking or even no cross-linking. Then the elevation of the dosage of aluminum glycinate increased the concentration of Al^{3+}, thereby enhancing the degree of cross-linking. Eventually, there was no significant change in the degree of cross-linking due to the limited ligand concentration. Cataplasms with 0.10% and 0.15% aluminum glycolate had similar $Force_{max\text{-}cat}$, mesh rate, crosslinking completion time, and adhesion properties (Fig. 9C−E, Fig. S13E−S13H, and Supporting Information Table S21).

As illustrated in Fig. 9F−K and Supporting Information Fig. S14A−S14G, the order of $Mean_{G'\text{-}LVR}$, $Force_{max\text{-}mid}$, $Force_{max\text{-}cat}$, and mesh rate was: aluminum hydroxide > aluminum glycolate > aluminum silicate. It was speculated that the main reasons for this result were the pH of the crosslinking agent, the molar amount of Al, and the bond energy between Al and O (Fig. S14H and Supporting Information Table S22). Specifically, the higher the pH of the crosslinking agent, the easier it was for the acidic pH modifier to dissociate Al^{3+} from the crosslinking agent. Additionally, cataplasms prepared with aluminum hydroxide had the highest molar amount of Al, resulting in a higher crosslinking degree and cohesive strength compared to cataplasms prepared with aluminum glycine or aluminum silicate. It was worth noting that, under the same pH, although the molar amount of Al in cataplasms prepared with aluminum silicate was greater than that with aluminum glycolate, the structural strength or cohesion of cataplasms prepared with aluminum glycolate was greater than that of aluminum silicate. The reason for this difference might be the bond energy between Al and O. The bond energy of the Al−O was lower than that of Al═O. Thus, Al^{3+} in aluminum glycolate was more easily dissociated, facilitating the formation of a cross-linked network and enhancing the cross-linking degree of the formulation. In addition, as shown in Fig. 9L, cataplasms prepared with aluminum silicate had the greatest adhesion.

$Mean_{G'\text{-}LVR}$, $Force_{max\text{-}mid}$, $Force_{max\text{-}cat}$, and mesh rate of cataplasms reflected its structural strength and cohesion. The poor cohesion of cataplasms led to non-formability when the amount of aluminum glycolate was at 0 and 0.05% (Supporting Information

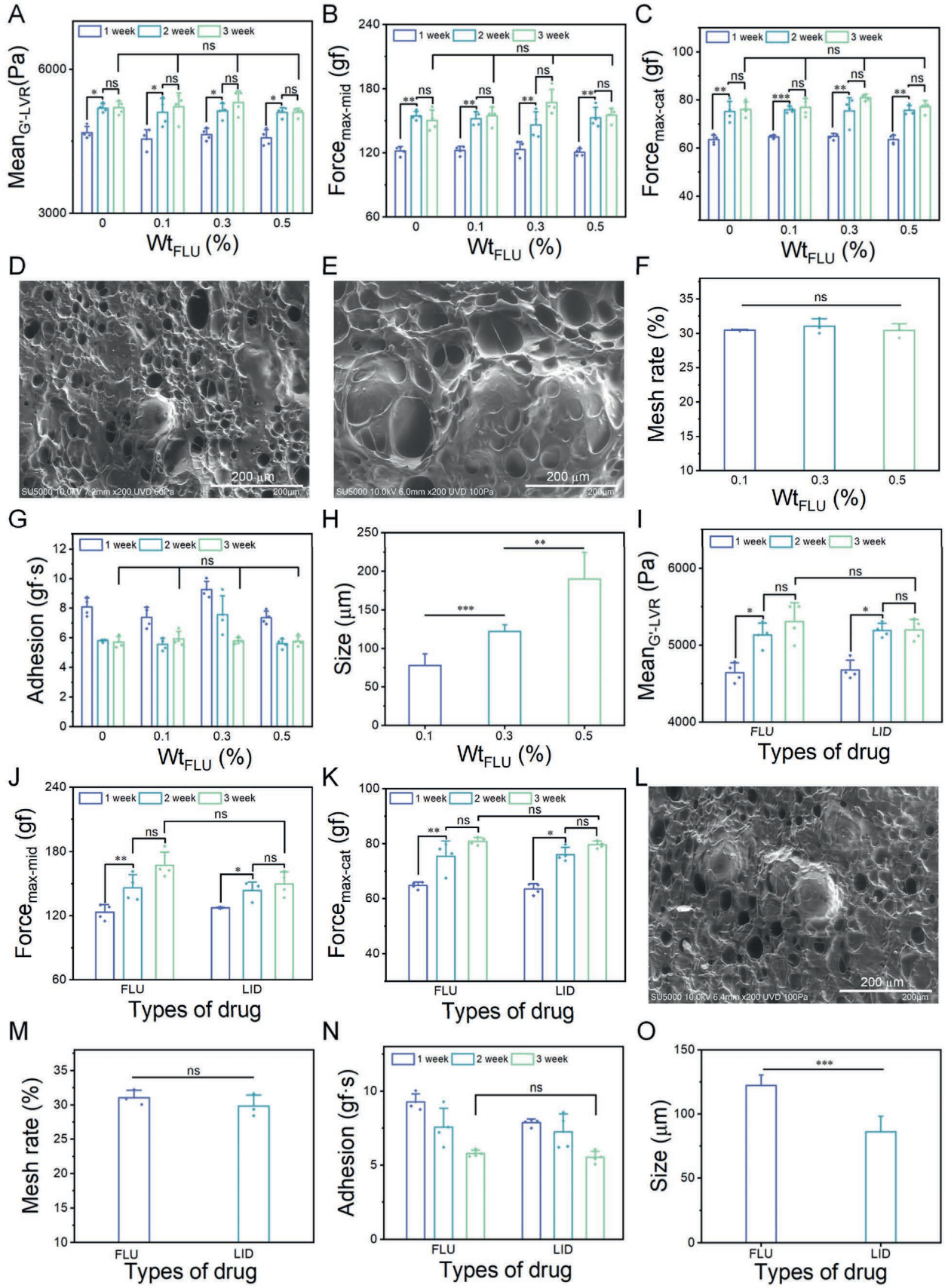

Figure 10 Structural characterization of cataplasms loaded with different drugs. Variation of (A) $Mean_{G'\text{-}LVR}$, (B) $Force_{max\text{-}mid}$, (C) $Force_{max\text{-}cat}$, and (F) mesh rate of cataplasms loading with different flurbiprofen dosages within 3 weeks. SEM images of cataplasms loaded with

Fig. S15A and S15B). The release film of cataplasms containing 0.10% aluminum glycolate could be peeled off intact. Moreover, it exhibited good formability (Fig. S15C−S15E). There was an important consideration here: the evaluation of formability required a minimum of 24.5 h, including 0.5 h of treatment at 37 °C/64% RH and 24 h of visual observation[53]. This process had taken a long time. Fortunately, established structural parameters, consisting of $Force_{max\text{-}mid}$, $Force_{max\text{-}cat}$, $Mean_{G'\text{-}LVR}$, and mesh rate, could be quickly detected. Based on a large amount of data in this study, when $Force_{max\text{-}mid} \geq 48.7 \pm 8.5$ gf, or $Force_{max\text{-}cat} \geq 25.8 \pm 1.3$ gf, or $Mean_{G'\text{-}LVR} \geq 2497.4 \pm 176.7$ Pa, or mesh rate $\geq 7.2 \pm 0.1\%$, cataplasms were considered to have good formability.

3.2.5. *Drugs*

There was a hydrophobic interaction between drugs and solubilizers, resulting in the formation of drug intermediates. As the dosage of flurbiprofen increased, it did not affect the degree of cross-linking in cataplasms. Therefore, there are no significant differences in $Mean_{G'\text{-}LVR}$, $Force_{max\text{-}mid}$, $Force_{max\text{-}cat}$, and mesh rate (Fig. 10A−F and Supporting Information Fig. S16). When the cross-linking process was fully completed, there were also no significant differences in adhesion and crosslinking completion time among different groups (Fig. 10G and Supporting Information Table S23). Notably, as the dose increased from 0.1% to 0.5%, the particle size of drug intermediates before and after pretreatment increased from 142.8 ± 0.9 nm to 673.6 ± 91.6 nm and 77.9 ± 14.9 μm to 190.0 ± 34.5 μm (Fig. 10H and Supporting Information Fig. S17A−S17C), respectively. Meanwhile, it could also qualitatively characterize the increase in the proportion of element F (Fig. S17D−S17J).

Similarly, it was observed from Fig. 10I−N and Supporting Information Fig. S18 that there were no significant differences in $Mean_{G'\text{-}LVR}$, $Force_{max\text{-}mid}$, $Force_{max\text{-}cat}$, mesh rate, and adhesion between different drug type groups over 3 w. Differences in drug type do not affect the cross-linking degree in the cataplasms. The particle size of lidocaine before and after pretreatment was lower than that of flurbiprofen (Fig. 10O and Supporting Information Fig. S19A), resulting from the lower hydrophobicity of lidocaine. Additionally, the N element proportion in the lidocaine group was higher than that in the flurbiprofen group (Fig. S19B−S19D), attributing to the fact that lidocaine contained N atoms that were absent in flurbiprofen. Although the secondary structure proposal had been validated, the limitation of this method was that it was difficult to perform qualitative characterization for drugs without distinct characteristic elements.

3.3. *Storage conditions*

As shown in Fig. 11A−I and Supporting Information Fig. S20, during the process of increasing relative humidity (RH) from 40% to 75% at 25 °C, there were no significant changes in $Mean_{G'\text{-}LVR}$, $Force_{max\text{-}cat}$, mesh rate, and adhesion within 2 weeks. However, under 75% RH, as the temperature increased from 25 to 60 °C, $Mean_{G'\text{-}LVR}$ and $Force_{max\text{-}cat}$ decreased by 37.5% and 31.7%, respectively. Generally, higher temperatures were more conducive to the formation of cross-linked networks. However, cataplasms contained multiple components, including various hydrophilic substances. This result was speculated to be due to the reduction in intermolecular forces caused by the increase in temperature[54,55], thereby lowering the cohesive strength of the paste. Although the mesh rate did not change significantly, the mesh appeared to show signs of damage. Meanwhile, after being stored at 40 and 60 °C for 2 weeks, the color of cataplasms changed from white to yellow (Supporting Information Fig. S21), indicating poor formulation quality, which also correlated with changes in structural parameters.

In addition, the selection of packaging quantity during storage had a certain impact on the cross-linked network structure. The higher the package count per unit, the greater the pressure exerted on the bottom of cataplasms when placed horizontally, resulting in a more significant structural impact. As shown in Fig. 11J−O and Supporting Information Fig. S22, increasing the number of cataplasms per package (from 2 to 8) did not alter the $Force_{max\text{-}cat}$, mesh rate, and adhesion over 4 m. This might be because cataplasms possessed a certain structural strength, enabling them to maintain their original structure under external force. By examining the dynamic changes in structure under different storage conditions, the stability of cataplasms can be assessed, further expanding the application of the tertiary structure.

In a word, in the process of storage under different conditions, it was helpful to evaluate the quality of cataplasms by investigating the dynamic structure.

3.4. *Correlation between structural parameters*

The main function of the cross-linked network structure was to provide sufficient cohesion for cataplasms, thereby endowing good formability. The parameters reflecting the cohesion of the formulation in its primary structure include $Mean_{G'\text{-}LVR}$, $Force_{max\text{-}mid}$, $Force_{max\text{-}cat}$, and mesh rate. Notably, as shown in Fig. 12, the R^2 values for the linear correlation between $Force_{max\text{-}mid}$ and $Mean_{G'\text{-}LVR}$, $Force_{max\text{-}cat}$, and mesh rate are 0.891, 0.915, and 0.837, respectively. These values collectively indicate that the structural parameters of the paste and cataplasms exhibited good correlation. This implied that detection of a constant plateau in any one of the $Mean_{G'\text{-}LVR}$, $Force_{max\text{-}mid}$, or $Force_{max\text{-}cat}$ confirmed crosslinking completion for cataplasms. Furthermore, combining the threshold values for key structural parameters from Part 3.2.4 allowed inference that when crosslinking was complete, the cohesive parameters of both the paste and cataplasms could be used to assess the formulation's formability. These relationships held practical significance for industrial applications.

(D) 0.1% and (E) 0.5% flurbiprofen. (G) Changes in adhesion of cataplasms with different flurbiprofen within 3 weeks. (H) Size of drug intermediates after pretreatment in cataplasms loaded with different flurbiprofen dosages. Variation of (I) $Mean_{G'\text{-}LVR}$, (J) $Force_{max\text{-}mid}$, (K) $Force_{max\text{-}cat}$, and (M) mesh rate of cataplasms with different crosslinking agent types within 4 weeks. (L) SEM images of cataplasms loaded with lidocaine. (N) Changes in adhesion of cataplasms with different crosslinking agent types within 4 weeks. (O) Size of drug intermediates after pretreatment in cataplasms loaded with different drug types. The data are expressed as mean ± SD. Statistical analysis was performed using a Student's *t*-test for comparisons between two groups. One-way ANOVA was applied for comparisons involving three or more groups. $n = 4$. ns, *, **, and *** represented $P > 0.05$, $P < 0.05$, $P < 0.01$, and $P < 0.001$, respectively.

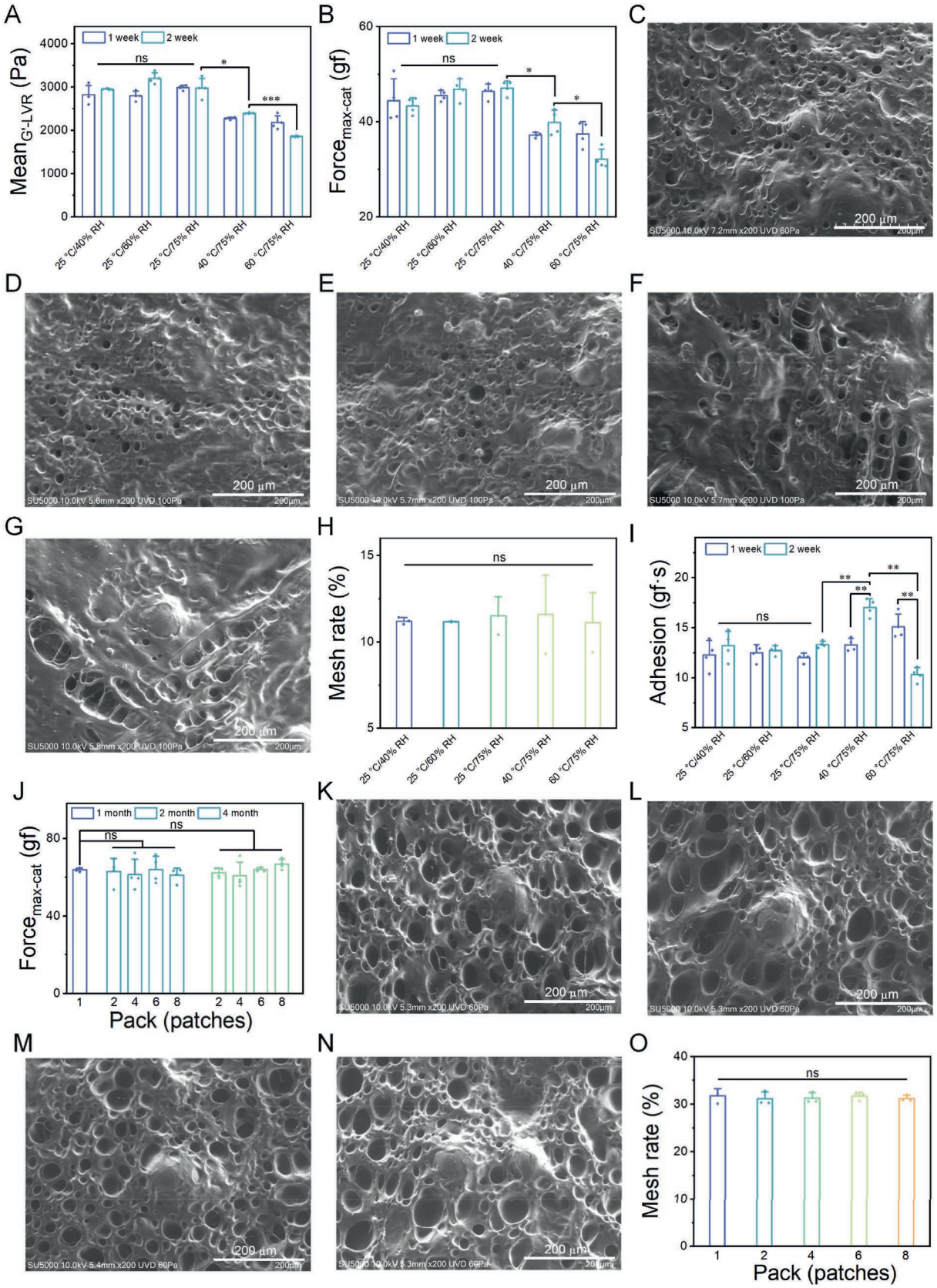

Figure 11 Structural characterization of cataplasms under different storage conditions. Variation of (A) $Mean_{G'\text{-}LVR}$, (B) $Force_{max\text{-}cat}$, and (H) mesh rate of cataplasms under different RH and temperature within 2 weeks. SEM images of cataplasms at (C) 25 °C/40% RH, (D) 25 °C/60% RH, (E) 25 °C/75% RH, (F) 40 °C/75% RH, and (G) 60 °C/75% RH. (I) Changes in the adhesion of cataplasms under different RH and temperature within 2 weeks. Variation of (J) $Force_{max\text{-}cat}$ and (O) mesh rate of cataplasms with different patches per pack within 4 months. SEM images of cataplasms with (K) 2, (L) 4, (M) 6, (N) 8 patches per pack. The data are expressed as mean ± SD. One-way ANOVA was applied for comparisons. $n = 4$. ns, *, **, and *** represented $P > 0.05$, $P < 0.05$, $P < 0.01$, and $P < 0.001$, respectively.

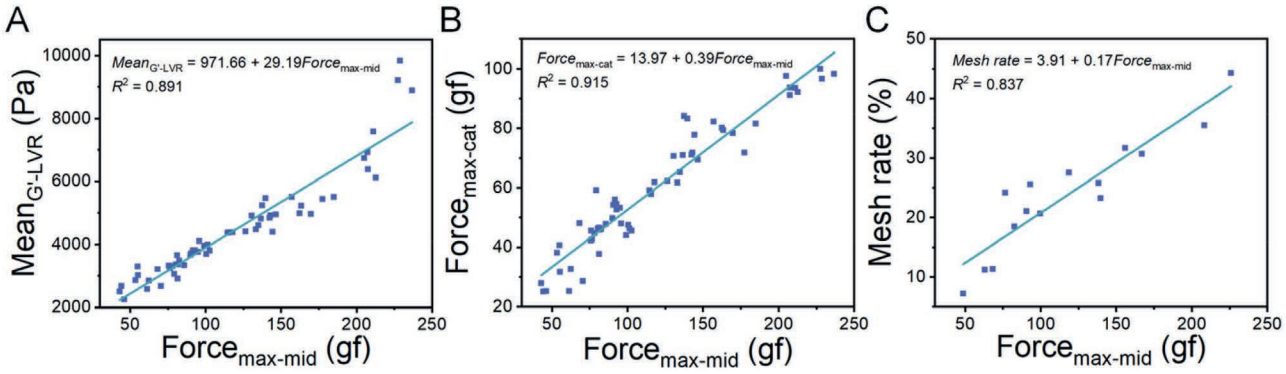

Figure 12 Correlation between structural parameters. Correlation between $Force_{max\text{-}mid}$ and (A) $Mean_{G'\text{-}LVR}$, (B) $Force_{max\text{-}cat}$, and (C) mesh rate.

4. Conclusions

In summary, we first proposed and systematically established structural parameters for emulsion-type cataplasms with cross-linked networks from a four-level structural perspective, offering new insights into the design of formulations. The validity of these structural parameters was further validated by altering key components, including gel skeleton, pH modifier, cross-linking regulator, cross-linking agent, and drug. It was worth noting that when $Force_{max\text{-}mid} \geq 48.7 \pm 8.5$ gf, or $Force_{max\text{-}cat} \geq 25.8 \pm 1.3$ gf, or $Mean_{G'\text{-}LVR} \geq 2497.4 \pm 176.7$ Pa, or mesh rate $\geq 7.2 \pm 0.1\%$, it indicated that time-consuming experimental validation of its excellent formability was unnecessary. The tertiary structure parameters could not only determine the maturation time of cataplasms but also effectively evaluate its stability. More importantly, the strong correlation among primary parameters demonstrated that quantitative assessment of cataplasms quality was achievable for both the structure characterization of paste and cataplasms, providing a new technical perspective for industrial development. However, there are still limitations, such as the expansion of parameter characterization methods at each level, particularly in the characterization methods for secondary structures. In the future, we will further refine and update this research, which is expected to promote the industrialization of cataplasms.

Acknowledgments

This work was supported by Changsha Jingyi Pharmaceutical Technology Co., Ltd. We sincerely thank Chen Chen from Changsha Jingyi Pharmaceutical Technology Co., Ltd., for his guidance on the preparation of cataplasms, and Ran Huang and Qixia Zhao from Changsha Jingyi Pharmaceutical Technology Co., Ltd., for their guidance on the use of SEM-EDS and soft ion polisher.

Author contributions

Peng Yan: Conceptualization, Data curation, Formal analysis, Investigation, Software, Methodology, Validation, Writing - original draft, Writing - review & editing. Ying Zhou: Data curation, Software, Visualization. Hailong Zhang: Methodology, Validation. Jinsong Ding: Conceptualization, Funding acquisition, Investigation, Project administration, Resources, Supervision, Writing - review & editing.

Conflicts of interest

The authors declare no conflicts of interest.

Appendix A. Supporting information

Supporting information to this article can be found online at https://doi.org/10.1016/j.apsb.2025.12.046.

References

1. Shen S, Liu SZ, Zhang YS, Du MB, Liang AH, Song LH, et al. Compound antimalarial ethosomal cataplasm: preparation, evaluation, and mechanism of penetration enhancement. *Int J Nanomed* 2015;**10**: 4239−53.
2. Gu X, Guo J, Mai Y, Niu Y, Chen J, Zhao Q, et al. Improved transdermal permeability of tanshinone IIA from cataplasms by loading onto nanocrystals and porous silica. *Pharmaceut Dev Technol* 2021; **26**:1061−72.
3. Yamauchi Hitoshi. Semi-solid and transdermal drug delivery systems-usefulness of patches for local and systemic action. *Oleoscience* 2017; **17**:559−65.
4. Miyazaki T, Kanno H, Yamamoto E, Ando D, Izutsu Ki, Goda Y. Cold flow evaluation in transdermal drug delivery systems by measuring the width of the oozed adhesive. *AAPS PharmSciTech* 2020;**21**:120.
5. Yang J, Zhu Y, Diao Y, Yin C. Rheological and mechanical analyses of felbinac cataplasms by using box−Behnken design. *Pharmaceutics* 2018;**10**:88.
6. Shao C, Wang M, Meng L, Chang H, Wang B, Xu F, et al. Mussel-inspired cellulose nanocomposite tough hydrogels with synergistic self-healing, adhesive, and strain-sensitive properties. *Chem Mater* 2018;**30**:3110−21.
7. Depalle B, Qin Z, Shefelbine SJ, Buehler MJ. Influence of cross-link structure, density and mechanical properties in the mesoscale deformation mechanisms of collagen fibrils. *J Mech Behav Biomed Mater* 2015;**52**:1−13.
8. Ramadon D, McCrudden MTC, Courtenay AJ, Donnelly RF. Enhancement strategies for transdermal drug delivery systems: current trends and applications. *Drug Deliv Transl Res* 2021;**12**:758−91.
9. Yamauchi Hitoshi, Goto Motoaki. Usefulness of pap preparation to improve quality of life (QOL) of patients. *Surf Sci* 2006;**27**:730−3.
10. Li D, Cheng Y, Yuan P, Wu Z, Liu J, Kan J, et al. Efficacy and safety of flurbiprofen cataplasms *versus* loxoprofen sodium cataplasms in knee osteoarthritis: a randomized controlled trial. *Chin Med J* 2023; **136**:2187−94.
11. Agarwal V, Singh SK, Reddy IK, Durrani MJ, Khan MA. Cataplasm-based controlled drug delivery: development and

optimization of a novel formulation. *Drug Dev Ind Pharm* 1999; **25**:659−65.
12. Hayashi T, Yamazaki T, Yamaguchi Y, Sugibayashi K, Morimoto Y. Release kinetics of indomethacin from pressure sensitive adhesive matrices. *J Control Release* 1997;**43**:213−21.
13. Xu H, Wu L, Xue Y, Yang T, Xiong T, Wang C, et al. Advances in structure pharmaceutics from discovery to evaluation and design. *Mol Pharm* 2023;**20**:4404−29.
14. Zhang S, Byrne G. Characterization of transport mechanisms for controlled release polymer membranes using focused ion beam scanning electron microscopy image-based modelling. *J Drug Deliv Sci Technol* 2021;**61**:194.
15. Sun X, Wu L, Maharjan A, Sun H, Hu X, York P, et al. Static and dynamic structural features of single pellets determine the release behaviors of metoprolol succinate sustained-release tablets. *Eur J Pharmaceut Sci* 2020;**149**:105324.
16. Yin X, Li H, Guo Z, Wu L, Chen F, de Matas M, et al. Quantification of swelling and erosion in the controlled release of a poorly water-soluble drug using synchrotron X-ray computed microtomography. *AAPS J* 2013;**15**:1025−34.
17. Yin X, Li L, Gu X, Wang H, Wu L, Qin W, et al. Dynamic structure model of polyelectrolyte complex based controlled-release matrix tablets visualized by synchrotron radiation micro-computed tomography. *Mater Sci Eng C* 2020;**116**:111137.
18. Yan P, Hou Z, Ding J. A review of research methods for elucidating the microstructure of pharmaceutical preparations. *J Pharm Anal* 2025;**15**:101156.
19. Zheng J, Xu H. Chapter 9—Formulation work for transdermal delivery systems. In: Zheng J, editor. *New transdermal drug delivery formulations*. Beijing: The People's Health Press Co., Ltd.; 2006. p. 366−70.
20. Ren Y, Yang K, Wang Z, Zhang Z, Chen Y, Shi X, et al. Substrate-free dissolving microneedles with barbed shape to increase adhesion and drug-delivery efficiency to skin. *J Control Release* 2024;**368**: 199−207.
21. Wang R, Zhou Y, Yan P, Zhang H, Ding J. A novel topical compound gel loading minoxidil and tofacitinib for treatment of alopecia areata: formulation, characterization, and *in vitro/in vivo* evaluation. *Drug Dev Res* 2025;**86**:e70076.
22. Chun MK, Hossain K, Choi SH, Ban SJ, Moon H, Choi HK. Development of cataplasmic transdermal drug delivery system containing eutectic mixture of lidocaine and prilocaine. *J Pharm Invest* 2012;**42**: 139−46.
23. Nathi R, Ketha NVDP, Kowtarapu LP, Muchakayala SK, Konduru N, Saroja B, et al. Flurbiprofen cataplasms: development and validation of *in-vitro* dissolution methods and evaluation of multimedia dissolution profiles. *Pharm Sci Adv* 2023;**1**:100018.
24. Tian J, Zhang X, Zhou X. A novel cataplasma matrix of traditional Chinese medicine. *Front Chem Eng China* 2010;**4**:91−5.
25. Wang J, Zhang H, An D, Yu J, Li W, Shen T, et al. Rheological characterization of cataplasm bases composed of cross-linked partially neutralized polyacrylate hydrogel. *AAPS PharmSciTech* 2014;**15**: 1149−54.
26. Liu L, Wang N, Xu LR, Yu XZ, Zhang R, Wang T. A novel method of determining wax cohesiveness by using a texture analyzer. *J Texture Stud* 2016;**47**:161−6.
27. Liu GD, Zhang C, Zhang SH, Liu XX, Luo JF, Gao H, et al. Simulated oral processing of cooked rice using texture analyzer equipped with multiple extrusion cell probe (TA/MEC). *Lwt-Food Sci Technol* 2021; **138**:110731.
28. Al-Smadi K, Ali M, Zhu JX, Abdoh A, Phan K, Mohammed Y. Advances in characterization of transdermal and topical products using texture analyzer systems. *AAPS PharmSciTech* 2025;**26**:157.
29. Terukina T, Muramoto S, Osanai K, Inoue M, Watanabe H, Hakamata Y, et al. Effect of liquid paraffin on the characteristics of pressure-sensitive adhesives applied to medical tape formulations. *J Pharm Innov* 2023;**18**:2110−9.
30. Hou Z, Wen Q, Zhou W, Yan P, Zhang H, Ding J. Topical delivery of ketorolac tromethamine *via* cataplasm for inflammatory pain therapy. *Pharmaceutics* 2023;**15**:1405.
31. Xue Y, Xu L, Wang A, Ma Y, Zhang W, Ji W, et al. Studying spatial drug distribution in golf ball-shaped microspheres to understand drug release. *J Control Release* 2023;**357**:196−209.
32. Li S, Lin J, Wang C, Liu J, Wang Y, Chen Y, et al. Synergistic metabolic modulation of fibroblast-like synoviocytes *via* targeted dual prodrug nanoparticles to mitigate rheumatoid arthritis. *Acta Pharm Sin B* 2025;**15**:542−56.
33. McAuley WJ, Chavda-Sitaram S, Mader KT, Tetteh J, Lane ME, Hadgraft J. The effects of esterified solvents on the diffusion of a model compound across human skin: an ATR-FTIR spectroscopic study. *Int J Pharm* 2013;**447**:1−6.
34. Zhang M, Jing H, Liu X, Milichko VA, Dou Y, Ren Y, et al. Intercellular communication interference through energy metabolism-related exosome secretion inhibition for liver fibrosis treatment. *Acta Pharm Sin B* 2025;**15**:4900−16.
35. Sliozberg Y, Andzelm J, Hatter CB, Anasori B, Gogotsi Y, Hall A. Interface binding and mechanical properties of MXene-epoxy nanocomposites. *Compos Sci Technol* 2020;**192**:108124.
36. Zhou L, Wang C, Ye Z, Yang F, Wang T, Zhang X, et al. Exploration of interactions of modified sodium lignosulfonate with coal pitch in coal pitch−water slurry based on experiments and simulations. *Colloids Surf, A* 2022;**647**:129063.
37. Basiuk VA, Borys-Sosa PA. Interaction of Au atom with fullerene C_{60}: performance of DFT functionals incorporated into the DMol3 module. *J Comput Theor Nanosci* 2013;**10**:328−33.
38. Song CJ, Jang CK, Yao W, Jaung JY. Synthesis and spectral characterisation of dicyanopyrazine-related cyanoheterocycles. *J Chem Res* 2013;**37**:268−72.
39. Yang L, Liu Q, Wang X, Gao N, Li X, Chen H, et al. Actively separated microneedle patch for sustained-release of growth hormone to treat growth hormone deficiency. *Acta Pharm Sin B* 2023;**13**: 344−58.
40. Simoes A, Miranda M, Cardoso C, Vitorino FVA. Rheology by design: a regulatory tutorial for analytical method validation. *Pharmaceutics* 2020;**12**:820.
41. Nasrazadani S, Hassani S. Chapter 2—Modern analytical techniques in failure analysis of aerospace, chemical, and oil and gas industries. In: ASH Makhlouf, Aliofkhazraei M, editors. *Handbook of materials failure analysis with case studies from the oil and gas industry*. Oxford: Butterworth-Heinemann; 2016. p. 39−54.
42. Axel Zeitler J, Rades T. Interdependence of dosage form microstructure and performance. *Pharm Res* 2017;**34**:887−9.
43. Förster H. UV/VIS spectroscopy. In: Karge HG, Weitkamp J, editors. *Characterization I*; 2004. p. 337−426. Berlin: Heidelberg.
44. Malakhovskii AV, Isachenko VA, Sukhachev AL, Potseluyko AM, Zabluda VN, Zarubina TV, et al. Magneto-optical properties of Dy^{3+} in oxide glasses: the origin of the magneto-optical activity of f−f transitions and its anomalous temperature dependence. *Phys Solid State* 2007;**49**:701−7.
45. Pharmaceuticals and medical devices agency. ZEPOLAS® PAP. Attached document. Published [May. 1988]. Updated [Oct. 2024]. Accessed [Oct. 2025]. Available from: https://www.pmda.go.jp/PmdaSearch/iyakuDetail/ResultDataSetPDF/750007_2649732S1164_1_09.
46. Pharmaceuticals and Medical Devices Agency. Catlep® Paps. Attached document. Published [Dec. 1989]. Updated [Oct. 2024]. Accessed [Oct. 2025]. Available from: https://www.pmda.go.jp/PmdaSearch/iyakuDetail/ResultDataSetPDF/470006_2649719S1185_1_07.
47. Pharmaceuticals and Medical Devices Agency. Seltouch® Paps. Attached document. Published [Sep. 1993]. Updated [Oct. 2024]. Accessed [Oct. 2025]. Available from: https://www.pmda.go.jp/PmdaSearch/iyakuDetail/ResultDataSetPDF/470006_2649731S1143_1_10.
48. Food and Drug Administration. LIDODERM®. Label. Published [Mar. 1993]. Updated [Nov. 2018]. Accessed [Oct. 2025]. Available from:

https://www.accessdata.fda.gov/drugsatfda_docs/label/2015/020612s012lbl.pdf.
49. Pharmaceuticals and Medical Devices Agency. NABOAL® Paps. Attached document. Published [Aug. 2006]. Updated [Jan. 2025]. Accessed [Oct. 2025]. Available from: https://www.pmda.go.jp/PmdaSearch/iyakuDetail/ResultDataSetPDF/650034_2649734S3042_1_13.
50. Pharmaceuticals and medical devices agency. LOXONIN® PAP. Attached document. Published [May. 2006]. Updated [Mar. 2025]. Accessed [Oct. 2025]. Available from: https://www.pmda.go.jp/PmdaSearch/iyakuDetail/ResultDataSetPDF/850028_2649735S1028_1_16 (Accessed October 17, 2025).
51. Food and Drug Administration. Flector® patch. Label. Published [Jan. 2007]. Updated [Nov. 2024]. Accessed [Oct. 2025]. Available from: https://www.accessdata.fda.gov/drugsatfda_docs/label/2007/021234lbl.pdf.
52. Pharmaceuticals and medical devices agency. MOHRUS® Paps XR. Attached document. Published [Dec. 2015]. Updated [Oct. 2024]. Accessed [Oct. 2025]. Available from: https://www.pmda.go.jp/PmdaSearch/iyakuDetail/ResultDataSetPDF/650034_2649729S5028_1_09.
53. Chinese Pharmacopoeia Commission. 0122 Tiegaoji. Chinese pharmacopoeia 2020 edition part IV. Published [Dec. 2020]. Updated [Oct. 2023]. Accessed [Oct. 2025]. Available from: https://ydz.chp.org.cn/#/item?bookId=4&entryId=5393.
54. Chen H, Qin F, Wang Y, Yu Z. Effect of complexation temperature on thermal properties and enzymatic hydrolysis of starch−oleic acid complexes. *Cereal Chem* 2017;**94**:237−41.
55. Mizan TI, Savage PE, Ziff RM. Temperature dependence of hydrogen bonding in supercritical water. *J Phys Chem* 1996;**100**:403−8.